LAWRENCE
LIVERMORE
NATIONAL
LABORATORY

LLNL-JRNL-653748

The Effects of Early Tme Laser Drive on Hydrodynamic Instability Growth in National Ignition Facility Implosions

J. L. Peterson, D. S. Clark, L. P. Masse, L. J. Suter

April 28, 2014

Physics of Plasmas

Disclaimer

This document was prepared as an account of work sponsored by an agency of the United States government. Neither the United States government nor Lawrence Livermore National Security, LLC, nor any of their employees makes any warranty, expressed or implied, or assumes any legal liability or responsibility for the accuracy, completeness, or usefulness of any information, apparatus, product, or process disclosed, or represents that its use would not infringe privately owned rights. Reference herein to any specific commercial product, process, or service by trade name, trademark, manufacturer, or otherwise does not necessarily constitute or imply its endorsement, recommendation, or favoring by the United States government or Lawrence Livermore National Security, LLC. The views and opinions of authors expressed herein do not necessarily state or reflect those of the United States government or Lawrence Livermore National Security, LLC, and shall not be used for advertising or product endorsement purposes.

The effects of early time laser drive on hydrodynamic instability growth in National Ignition Facility implosions

J. L. Peterson[1], D. S. Clark[1], L. P. Masse[2], L. J. Suter[1]
1 *Lawrence Livermore National Laboratory, Livermore, California 94550, USA and*
2 *CEA, DAM, DIF, 91297 Arpajon, France*

Defects on inertial confinement fusion capsule surfaces can seed hydrodynamic instability growth and adversely affect capsule performance. The dynamics of shocks launched during the early period of x-ray driven National Ignition Facility (NIF) implosions determine whether perturbations will grow inward or outward at peak implosion velocity and final compression. In particular, the strength of the first shock, launched at the beginning of the laser pulse, plays an important role in determining Richtmyer-Meshkov (RM) oscillations on the ablation front. These surface oscillations can couple to the capsule interior through subsequent shocks before experiencing Rayleigh-Taylor (RT) growth. We compare radiation hydrodynamic simulations of NIF implosions to analytic theories of the ablative RM and RT instabilities to illustrate how early time laser strength can alter peak velocity growth. We develop a model that couples the RM and RT implosion phases and captures key features of full simulations. We also show how three key parameters can control the modal demarcation between outward and inward growth.

I. INTRODUCTION

Understanding the hydrodynamic mixing of inertially confined fusion capsules is an important aspect of achieving ignition and gain on the National Ignition Facility (NIF) [1–3]. In particular, perturbations initially on the capsule ablator surface can grow and penetrate the interior of the capsule. Should such material reach the centrally forming deuterium-tritium (DT) hotspot, it could cool the center and threaten ignition. Indeed, by measuring the radiation emitted during capsule compression and burn, experiments on NIF have found evidence of ablator material reaching the hotspot [4, 5]. That is, mix occurs in NIF capsules. The salient issues are why, how much, and how to control it.

Mix in NIF implosions is driven by the interaction of multiple hydrodynamic instabilities, in particular, the shock-driven Richtmyer-Meshkov (RM) [6, 7] and the acceleration-driven Rayleigh-Taylor (RT) [8, 9] instabilities. When a capsule surface defect is shocked, it sends a rippled shock into the interior of the capsule. This rippled shock can imprint itself on the interface between the fusion fuel and the ablator material, where the RM instability causes the now-rippled interface to grow. The complication is that NIF designs incorporate multiple (typically 2-4) shocks [10]. As the perturbation on the fuel-ablator interface is growing, the shaped laser pulse launches additional shocks into the capsule, which each re-shock the interface. After the shocks, the laser power increases, and the capsule rapidly compresses. This strong acceleration can make the system unstable to RT growth, which will amplify any perturbations seeded by the shocks. By peak implosion velocity, RT is expected to amplify RM-seeded perturbations by several thousand times.

Experiments on NIF implosions have shown that during capsule acceleration the growth of artificially large perturbations (10x larger than typical) is linear or only weakly nonlinear [11]. Therefore, a useful metric for the early phase growth of surface perturbations is the linear regime growth factor [12–14], which is the ratio of the amplitude of a perturbation at the time of peak implosion velocity relative to its initial seed amplitude. These are often calculated by radiation-hydrodynamic simulations of either single linear eigenmodes or multi-mode perturbations decomposed into linear eigenmodes. Although the simulated perturbations are small enough to remain linear during the entire simulation, the convolution of their linear growth factor with a measured capsule surface has been shown to closely follow the results of three-dimensional (3D) nonlinear simulations of realistic surface growth [15]. During capsule deceleration, however, the 3D simulations can become highly nonlinear, and possibly inject ablator material into the forming hotspot. But prior to this time, a linear analysis does well to capture the evolution of realistic perturbations.

Because both experiments on artificially large perturbations and 3D simulations of realistic perturbations tend to follow linear behavior, the linear growth factor is a reasonable and economical way to estimate the expected growth of capsule perturbations during acceleration. Therefore, the growth factor can be used to set engineering specifications on capsule finishes [10]. In this analysis, the sign of the growth factor is important for determining the threat level of a particular capsule defect. If the growth factor is positive, an initially outward surface defect will predominantly grow outwards during the implosion. However, if the sign is negative, that defect can invert, penetrate into the capsule interior and push towards the central hotspot. The same is true for inward surface defects that have a positive growth factor. Such inward going growth is thought to be much more threatening to ignition, because it brings ablator material in towards the DT fuel.

Simulations of isolated defects only mix ablator material into the implosion hotspot during stagnation if they have grown inward and penetrated the dense shell prior to interacting with the returning stagnation shock. In such cases the rebounding shock can collide with the penetrating jet and cause it to turbulently mix with the surrounding DT. While this deceleration growth process is nonlinear (due to the re-shocking by the return shock), the growth of the defect until peak fuel velocity tends to remain linear. A surface defect that linearly grows inward during capsule acceleration is more likely to bring ablator material into the forming hotspot during capsule deceleration and stagnation. Specifically, the larger the linear growth of the defect during acceleration, the more likely it is to nonlinearly mix into the hotspot during deceleration. That is, the amount of ablator material that a particular surface defect can bring into the hotspot depends on the initial size of the defect, its modal content and its growth factor. Capsules are accepted or rejected in part by the simulated sum of all the penetrating material from all of their defects.

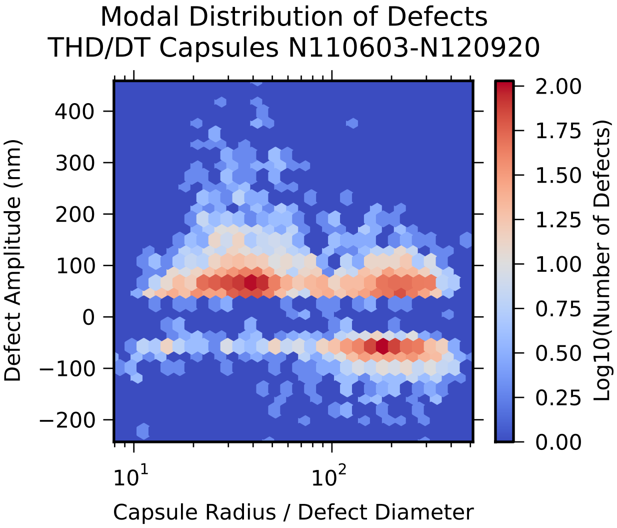

FIG. 1: Histogram of capsule surface defect sizes for all THD and DT NIF shots N110603-N120920.

Figure 1 shows a histogram of all of the isolated capsules defects found on all NIF DT and THD capsules shot during the National Ignition Campaign between June 3, 2011 and September 20, 2012. The defect amplitude (height) can be either positive (facing outward) or negative (facing inward). The ratio of the capsule radius to the defect diameter gives an estimate of the defects' approximate modal content. The vast majority of defects are positive, outward facing bumps, with a width distribution centered around roughly 1/40 the capsule radius (or about 30 μm). In fact, there are very few negative defects at these lower modes. At higher modes, the distribution is more symmetric around a small amplitude (the sharp horizontal boundaries indicate instrumental resolution; defects below this size are counted as general surface roughness and not isolated defects).

Since growth factor curves have been shown to accurately characterize the growth of these isolated defects, it is important to understand the features and behaviors of growth factor simulations. Simulated peak velocity growth factor curves for NIF designs tend to be positive at lower modes and negative at higher modes [10]. The location of this transition has implications, because of all of the defects represented in Figure 1, only those whose product of their amplitude and growth factor is negative are thought to contribute to mix. That is, the vast majority of defects, with the lower modal content, are presently calculated to benignly grow outward. Implosion features that move the positive-negative growth factor boundary have the potential to significantly alter the amount that a capsule mixes.

One such feature is the strength of the first shock, as determined by the amplitude of the first part of the laser drive, the "picket." In developing the NIF point design, one goal was to keep the growth factor curve positive for lower modes. When experimenting with different laser pulses, it was found [12, 14] that increasing the strength of the first shock moved the positive-negative growth factor transition from higher modes to lower modes. A higher picket meant that more of the lower-mode bumps would have negative growth factors, invert and grow into the capsule. For this (and other) reasons, the design team settled on a lower first shock strength, which kept negative growth factors at higher mode number.

While the sensitivity of the "growth factor zero" location at peak velocity was speculated to be due to different early-time RM physics, the exact mechanism for the change was largely left unexplored. In an attempt to better understand growth factor simulations, this work bridges the gap between the launch of the first shock and peak implosion velocity and investigates how altering the laser picket in growth factor simulations changes the temporal evolution of the RM and RT instabilities. We focus on the RM/RT-driven short wavelength perturbations, which are distinct from the longer wavelength perturbations driven by hohlraum radiation asymmetries. These low modes are also very important and can substantively harm performance [16] but are driven by a different mechanism. In essence, we find that the first shock sets up an ablative RM perturbation, from which subsequent shocks are launched. The later shocks carry that surface perturbation into the capsule. This process strongly couples the growth at the ablation front with the growth on interior capsule surfaces, even before RT growth sets in.

Section II details our simulation methodologies, the results of which appear in Section III. We compare the simulation results to existing analytic theory in Section IV, in which we also develop a model for coupled RM-RT growth. Section V contains a summary of the present and future work.

II. METHODOLOGY

To investigate how the first shock changes growth factors at peak velocity, we simulate the growth of the Rev5 Germanium-doped CH NIF capsule [10], a schematic of which appears in Figure 2. Growth factor simulations are done with the radiation hydrodyamics code HYDRA [17]. We compare three laser pulses, each characterized by a frequency dependent source, the radiation temperatures of which are shown in Figure 3. The solid line is a low picket version, the dashed line is the nominal Rev5 point design, and the dash-dot line is a high picket version. The low and high versions have had the launch times of shocks 2-4 shifted to give similar one-dimensional capsule performance. As shown in Figure 4, the first three shocks all coalesce near the ice-gas material interface and send a strong rarefaction fan back

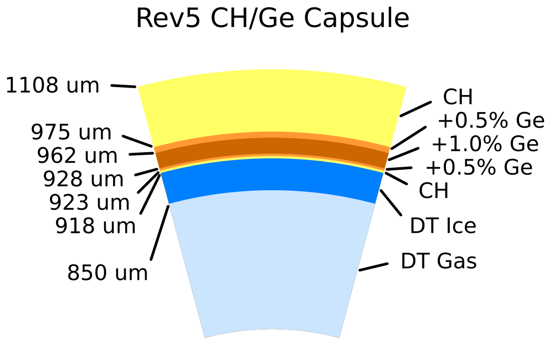

FIG. 2: A schematic of the Rev5 capsule with a CH ablator and Ge doped layers.

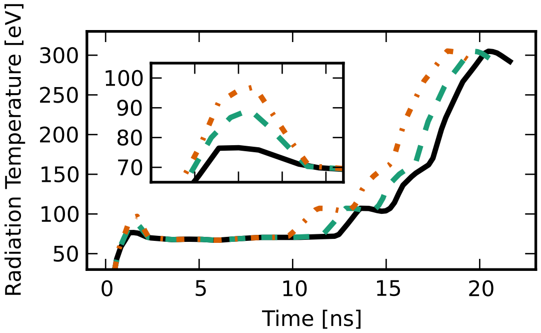

FIG. 3: Radiation temperatures for the three laser pulses with a low, nominal and high picket. Inset: zoom of the pickets for the three pulses.

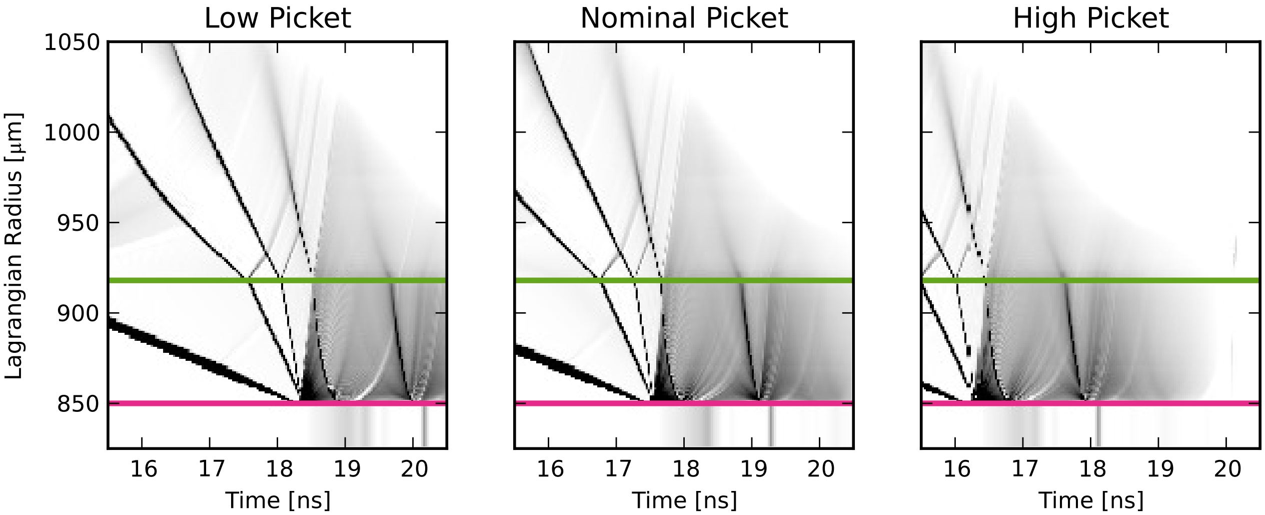

FIG. 4: Lagrangian shock plots of the logarithmic radial derivative of pressure for the three laser pulses with a low, nominal and high picket. The thick lines mark the locations of the gas-ice and ice-ablator interfaces.

towards the ablation surface. The fourth shock is timed to enter the fuel as the leading edge of that rarefaction fan enters the ablator. In all cases, a strong inward-going pressure wave emerges from the reflection of this fan off the ablation surface, turning into a fifth "shock" that can be seen transiting the DT ice layer at roughly 19 ns for the nominal picket.

The effects of these different laser pulses can be seen in Table I, a comparison of RT-relevant one-dimensional parameters at the time of peak implosion velocity. Within uncertainties, which are estimated from temporal resolution, the three laser pulses' one-dimensional parameters are comparable.

TABLE I: Comparison of RT-relevant one-dimensional implosion parameters for the three laser pulses at peak velocity. Uncertainties are estimated from finite simulation time resolution.

Picket Strength	Low	Nominal	High	Uncert.
Time of Peak Velocity [ns]	21.90	21.05	19.75	±0.05
Implosion Velocity [km/s]	-366.0	-367.0	-367.0	±0.5
Fuel Entropy [kJ/g/eV]	465	460	470	±5
Ablation Front Scale Length [μm]	12	11	10	±4
Fuel-Ablator Atwood Number	0.13	0.14	0.12	±0.01
Fraction of Ablator Mass Remaining	0.109	0.109	0.109	±0.002

The HYDRA growth factor simulations are all capsule-only simulations in cylindrical geometry of either single Legendre mode perturbations or multi-mode polar Gaussian bumps on the surface of the CH ablator. Diffusion is used for radiation transport, and the simulations remain Lagrangian through peak implosion velocity.

Growth factors are defined in terms of the Lagrangian radial amplitude perturbation. That is, we determine the perturbation δr at the radial mass coordinate r_m, angle θ and time t as the deviation from the average amplitude for all cells at the same radial mass coordinate r_m:

$$\delta r(r_m,\theta,t) = r(r_m,\theta,t) - \bar{r}(r_m,t). \tag{1}$$

In the case of a single mode of number l, the growth factor at mass coordinate r_m and time t, $\eta(l,r_m,t)$, is

$$\eta(l,r_m,t) = \frac{\delta r(r_m,\pi/2-\pi/\sqrt{l(l+1)},t) - \delta r(r_m,\pi/2,t)}{\delta r(r_c,\pi/2-\pi/\sqrt{l(l+1)},0) - \delta r(r_c,\pi/2,0)}. \tag{2}$$

The capsule outer surface is initially at a radius r_c, perturbed as a cosine from $\pi/2$ to $\pi/2 - \pi/\sqrt{l(l+1)}$ radians. Each single mode has an initial amplitude of 1/100 nm and contains 32 angular zones. The capsule is divided into 600 radial mass zones.

Multi-mode simulations are first decomposed in terms of Legendre modes and the amplitude of each mode compared to the amplitude of that mode at the capsule surface at the beginning of the simulation. The amplitude C of mode l at r_m and time t is

$$C(l, r_m, t) = \frac{2l+1}{2} \int \delta r(r_m, \theta, t) P_l(\cos\theta) d(\cos\theta), \tag{3}$$

where P_l is the l Legendre polynomial. The growth factor for mode l is

$$\eta(l, r_m, t) = \frac{C(l, r_m, t)}{C(l, r_c, 0).} \tag{4}$$

The Gaussian bumps have an initial height of 10 nm and width of 30 μm on the surface of the capsule, at mean radius 1108 μm, so that

$$\delta r(r_c, \theta, 0) = 10 \exp\left(-\left[\theta \frac{1108}{30}\right]^2\right) \text{ nm.} \tag{5}$$

The angular resolution is 512 zones over 30 degrees, but the bump simulation does not have equal angular resolution for each mode. At this resolution, a Legendre mode l spanning $180/l$ degrees would contain $3072/l$ zones. As the mode number increases, the resolution for that mode drops, and a single Legendre mode calculation is better representative of the linear growth factor.

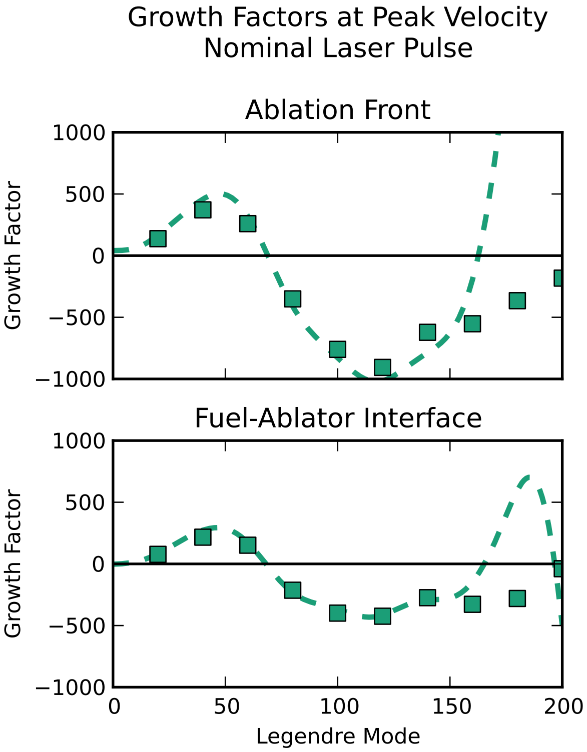

FIG. 5: Growth factor spectra at the ablation front (top) and the fuel-ablator interface (bottom) at peak velocity for the nominal picket pulse. The dashed line is from a simulation of a 30-degree multimode Gaussian bump decomposed in Legendre mode, and the squares are from single Legendre mode calculations. The single mode and multimode calculations agree for modes less than approximately 140.

Figure 5 shows the growth factor spectra on the ablation surface (as defined as the location of the maximum radial logarithmic derivative of the radiation temperature) and the fuel-ablator interface at the time of peak velocity for

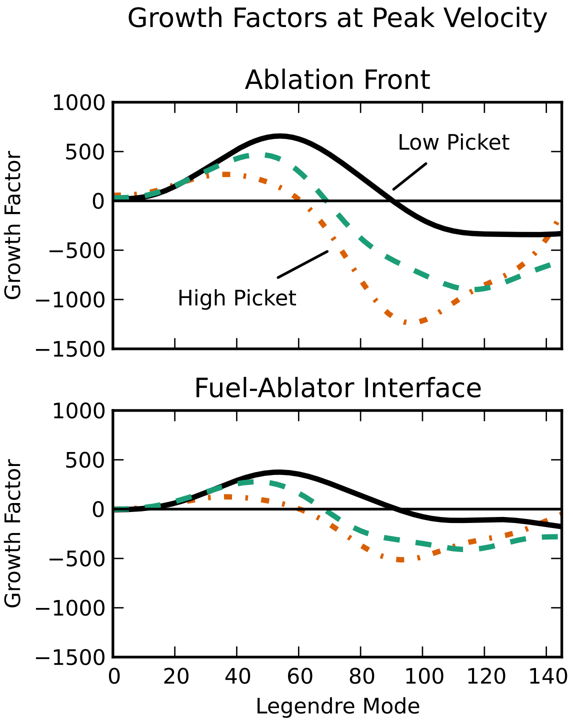

FIG. 6: Peak velocity growth factor spectra at the ablation front and fuel-ablator interface for the three capsule drives

the nominal picket drive. These spectra show that the bump simulations diverge from the single mode simulations at modes higher than approximately 150, and that both methods for calculating the growth factor agree at mode numbers below this threshold. Figure 5 also shows that the boundary conditions do not appreciably alter the single mode or the multimode bump growth factor simulations, because the bump simulations that can resolve multiple interacting modes on its thirty-degree angular domain agree with the single mode calculations of varying angular widths that inhibit coupling to longer-wavelength modes. (A convergence study showed that although simulations on a fifteen-degree domain showed some interaction with the domain boundary, the bump remained isolated from the boundary in a thirty-degree domain.) The agreement in Figure 5 comes not only from the wide angular domain and high angular resolution of the multimode simulation, but also from the small 10 nm initial bump perturbation.

III. SIMULATION RESULTS

The strength of the laser picket can influence peak-velocity growth factors at both the ablation front and the fuel-ablator interface. Figure 6 shows the growth factor spectra for the three capsule drives. Higher pickets have zero growth at lower mode number. The drive with the low laser picket has positive growth for modes below ~ 90, while the high picket drive has positive growth for modes below ~ 60. This zero-crossing location is the same at both the ablation front and the fuel-ablator interface, and the growth is larger for all modes at the ablation front than at the fuel-ablator interface.

However, the growth factor spectra seen at peak velocity are not the same as found earlier in the implosion. Growth factors during the capsule implosion are very dynamic, changing dramatically between the launch of the first shock and the time of peak implosion velocity. This is true for all three laser pulses, and the same patterns appear in the nominal Rev5 design as do in the other pulses.

Figure 7 shows the evolution of the growth factor at the ablation front in both mode number and time for the multimode simulation of the nominal laser pulse. The temporal evolution is divided into two epochs. The first, before the dotted line at 18 ns, involves a gradual sweeping of the growth factor zero location, marked by the solid black line, from higher mode number at early time to lower mode number at later times. Modes to the right of this line

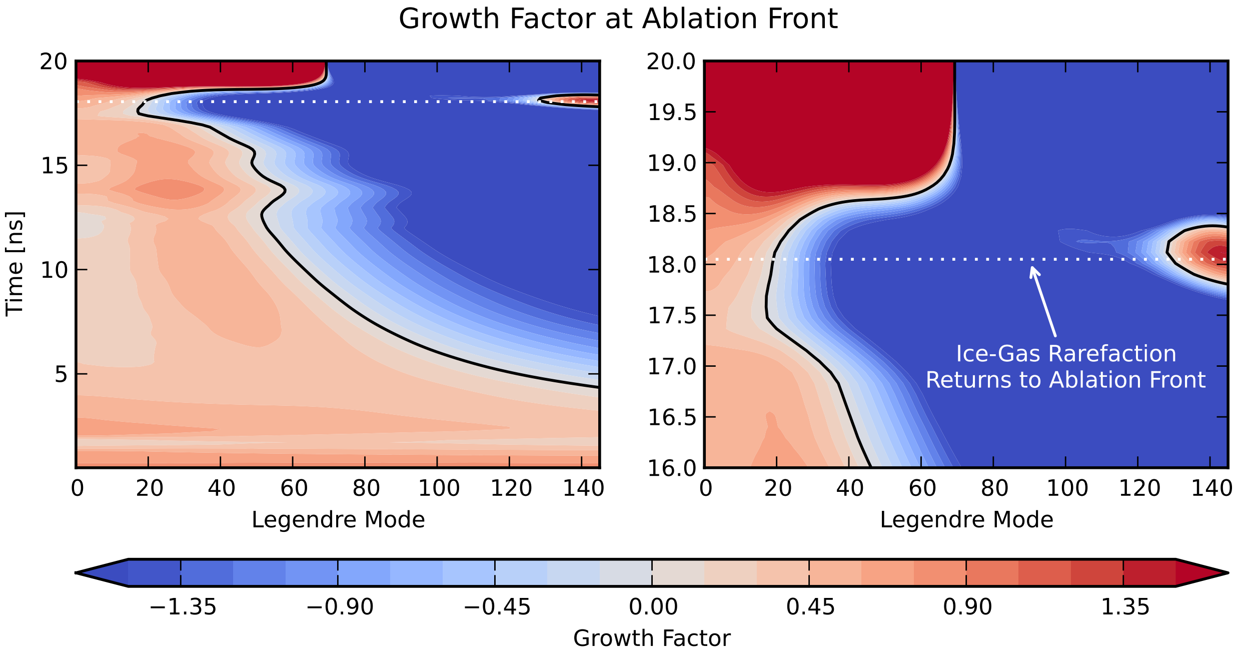

FIG. 7: Growth factor at the ablation front as a function of mode number and time for the nominal picket pulse at all times up to 20 ns (left) and a zoom of late times (right). The thick black line marks the zero contour, and the dotted line marks the time when the leading edge of the ice-gas rarefaction fan returns to the ablation front.

have a negative growth factor, while modes to the left are positive. The brief changes in the zero location at 13, 15 and 17 ns correspond to the launching of the second, third, and fourth shocks.

As seen in Figure 4, shocks 1, 2 and 3 combine into a strong shock, which creates an outward going rarefaction fan when it enters the DT gas. At the time indicated by the dotted line, the leading edge of this fan reaches the ablation surface. After this time, the growth factor zero changes trajectories and starts to move towards higher mode number. At late times ($t > 19$ ns), the sign of the growth factor is fixed for all modes until peak velocity. But the growth factor that appears at the ablation surface at peak velocity does not settle until very late in the implosion. It is worth noting that, as compared to the growth factors at peak velocity in Figure 6, these early time growth factors in Figure 7 are very small, but their signs match those that appear at peak velocity.

The trajectory of the zero-growth contour depends on the laser picket. Figure 8 shows the demarcation between positive and negative growth for the three capsule drives. All trajectories show the same dual-epoch behavior, separated by the return of the ice-gas rarefaction. Additionally, increasing the laser picket moves the zero-contour trajectory to lower mode numbers during the entire implosion, not just at peak velocity. All pulses also show brief periods of positive growth (near mode 140, for $t > 15$ ns), which appear after the launch of shock 4, but disappear before the end of the pulse.

The growth factor spectrum at the fuel-ablator interface is also temporally dynamic, as shown in Figure 9. The first shock enters the DT fuel layer near 13 ns and imprints the fuel-ablator interface with a growth factor. Each subsequent shock modifies the fuel-ablator growth factor as it transits the interface, and after the fifth shock, only a single zero-crossing exists. This zero is near mode 70 and is the same mode that is on the ablation surface at peak velocity. However, the zero mode is fixed at the fuel-ablator interface when shock 5 transits, before 19 ns (shock 4's transit near 18.5 ns fixes the lowest modes' sign, but the higher modes continue to evolve until shock 5 passes), but Figure 8 shows that the zero at the ablation surface continues to evolve until close to 19.5 ns. That is, shock 5 sets and fixes the sign of the growth factor at the fuel-ablator interface before the growth factor sign is settled at the ablation surface.

Just as the growth factors at the fuel-ablator interface change with shock transit, so do the growth factors at other parts of the capsule interior. Figure 10 shows snapshots of the DT ice and ablator for the high and low picket cases by plotting the growth factor as a function of Lagrangian radius at the launching of shocks 2, 4 and 5, as well as at peak velocity. The vertical lines mark the boundaries of the ablator, from the fuel-ablator interface on the left to the ablation front on the right. Numbers identify transiting shocks.

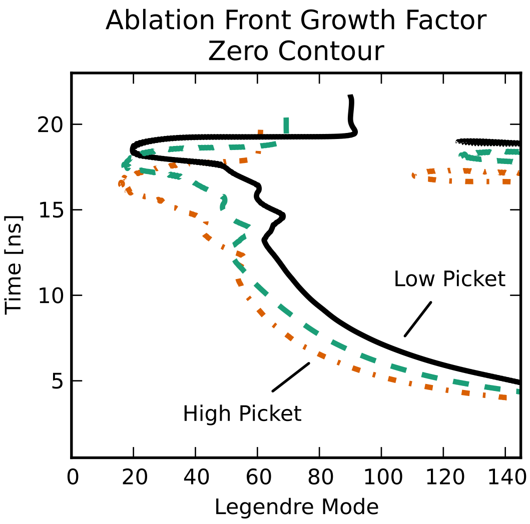

FIG. 8: Ablation front growth factor zero contour for the three laser drives.

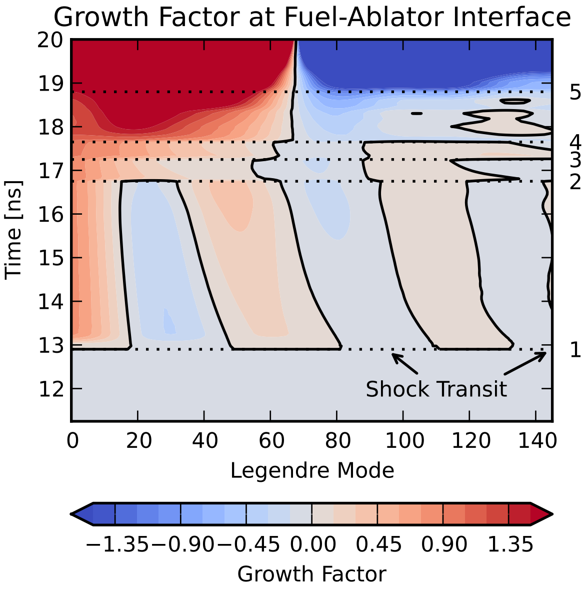

FIG. 9: Growth factor at the fuel-ablator interface as a function of mode number and time for the nominal picket pulse. The thick black line marks the zero contour. The dotted lines mark the transit times of shocks 1-5. Growth factors are zero before the first shock arrives.

Shocks 2, 4 and 5 are all launched from ablation surfaces with growth factors that are more positive for the low picket pulse than for the high picket pulse. In both cases, shock 2 [as seen by the labeled discontinuities in panel (b)], reduces the growth factor set up by shock 1 (that is, it adds negatively to it), but the change is greater for the high picket pulse (of about -0.5) than for the low picket pulse (of less than -0.1). Shock 4 also changes the growth factors in the capsule, so that by the time of the shock 5 launch [panel (c), corresponding to the start of main shell acceleration] the capsules exist in two different states: near zero for the high picket case and positive for the low picket

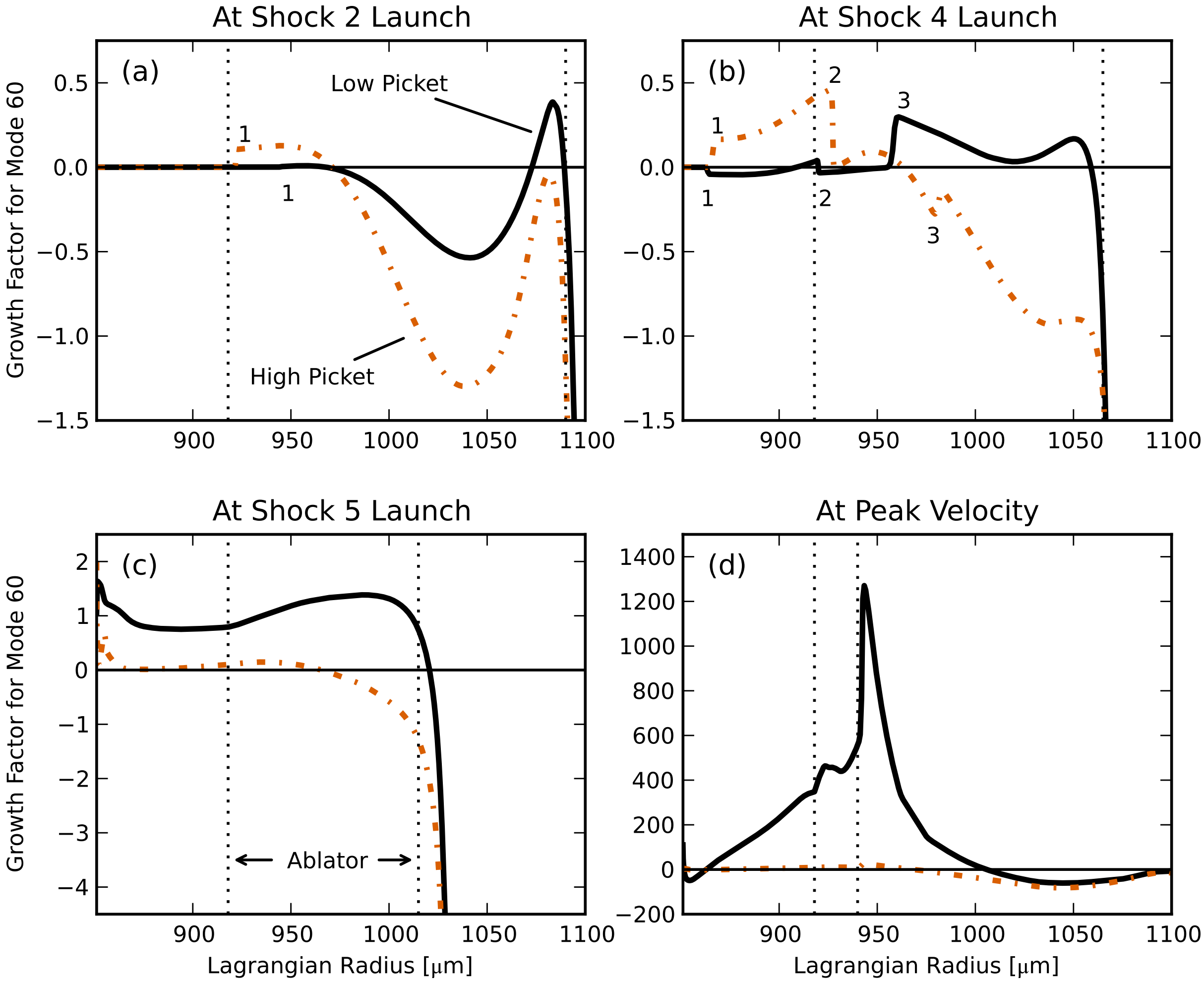

FIG. 10: Growth factors as a function of radius for mode 60 at different times for the low picket (solid) and high picket (dash-dot) pulses. Dotted lines mark the extent of the ablator, from the fuel-ablator interface on the left to the ablation surface on the right. Numbers identify transiting shocks.

case. This pattern carries through to peak velocity [panel (d)], by which time mode 60 grows to be very large for the low picket, but remains near zero for the high picket.

In essence, the simulations show that shocks launched from the ablation surface collectively perturb the capsule interior. During the main acceleration phase the ablation front moves through a perturbed capsule interior, which is not necessarily perturbed in the same fashion as the ablation surface. Changing the laser early in time changes how the shocks alter the state of the capsule interior later in time.

IV. COMPARISON TO ANALYTIC THEORY

One can interpret the behavior of the growth factor simulations in the context of analytic RM and RT theory, as applied to inertial confinement fusion targets.

Figure 9 shows that the fuel-ablator interface is initially perturbed by an oscillatory pattern when transited by shock 1. An initially uniform shock will oscillate with a frequency that depends on its mode number and the post-shock sound speed. In the strong shock limit in planar geometry [18], the growth factor η of a single mode k evolves according to

$$\eta = \eta_0 \frac{\sin\left(kc_s t\right)}{kc_s t}, \tag{6}$$

where c_s is the post-shock sound speed, and $\eta_0(l)$ is the shock's initial growth factor, which is 1 for the first shock. For our simulations, the post-shock sound speed is approximately $10 - 15$ μm/ns. To connect the planar result, Eq. 6, to cylindrical geometry, let $k = l/R$, where $R \approx 1100$ is the capsule radius. Figure 11 plots the simulated nominal drive growth factor of a characteristic following shock 1 alongside the theoretical early-time RM oscillations of the first shock, assuming a fixed value of R. Like the growth factor along shock 1 in the nominal picket simulation, the theoretical result oscillates with a period of about 2 ns, and damps at roughly the same rate, despite the assumption of fixed R. In other words, the shocks in our simulations evolve in a manner that is consistent with RM shock oscillations. Equation 6 can estimate the growth factor of each shock, assuming a given initial state $\eta_0(l)$, as set by the ablation surface.

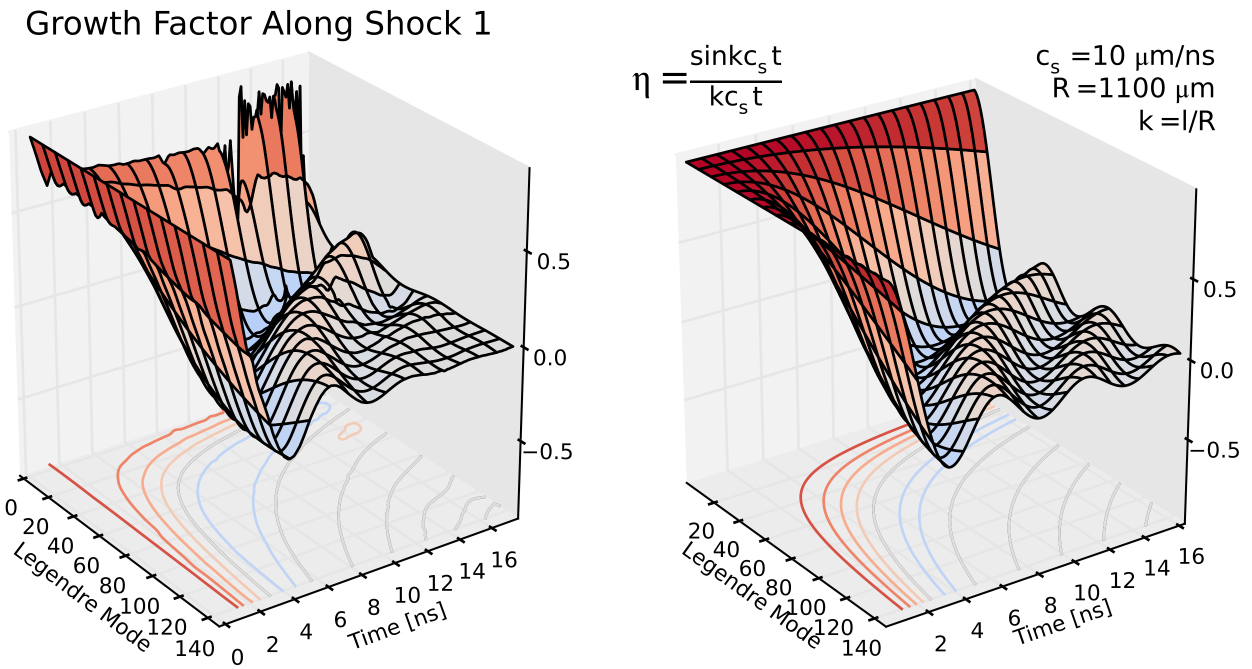

(a) Simulation

(b) Theory

FIG. 11: Simulated growth factor of a characteristic following shock 1 (a) and theoretical shock oscillations (b) for the nominal picket drive.

Unlike the shocks, the RM oscillations on the ablation surface are partly stabilized by mass ablation. Those oscillations are stabilized by the "dynamic overpressure" of modulations in the blow-off plasma [18]. The full ablative RM theoretical description of the early-time growth at the ablation front is given by η_{ARM}, as described by Eq. A24. For approximations that are valid for our simulations (see Appendix), the ablative RM growth factor becomes explicitly

$$
\begin{aligned}
\eta_{\mathrm{ARM}}(k,t) = \frac{20}{27}\left[\int_0^{kc_st} dt' \int_0^{t'} dt'' J_0(t'') + J_0(kc_st) - kc_st\right] + \frac{8}{27}\frac{J_1(kc_st)}{kc_st} \\
+e^{-2kV_at}\left[\left\{\frac{1}{9} + \frac{376}{729}\frac{c_s}{V_b}\right\}\cos\left(kt\sqrt{V_aV_b}\right)\right. \\
\left. + \left\{\frac{20}{27}\frac{c_s}{\sqrt{V_aV_b}} + \sqrt{\frac{V_a}{V_b}}\left[-\frac{16}{9} - \frac{V_b}{c_s} + \left(\frac{295}{243}\right)\frac{c_s}{V_b}\right]\right\}\sin\left(kt\sqrt{V_aV_b}\right)\right] \\
-\frac{8\sqrt{3}}{9}\frac{c_s}{V_b}e^{kV_at}\int_{kV_at}^{\infty} e^{-\tau}\left[J_1\left(\sqrt{3}\tau\right) + \frac{13}{27}J_3\left(\sqrt{3}\tau\right)\right] d\tau
\end{aligned}
\tag{7}
$$

The important parameters determining the growth at the ablation front are the post-shock sound speed, c_s, the ablation velocity V_a and the velocity of the blow-off plasma V_b. J_n are Bessel functions. The blow-off velocity depends on the ablation velocity, the wave number, the width of the ablation front L_0 and the conduction exponent ν:

$$
V_b = \frac{V_a}{\mu\left(kL_0\right)^{1/\nu}}. \tag{8}
$$

where

$$
\mu = \frac{(2/\nu)^{1/\nu}}{\Gamma\left(1+1/\nu\right)} + \frac{0.12}{\nu^2}. \tag{9}
$$

$\Gamma(x)$ is the Gamma Function, and for radiation-driven systems, $\nu \simeq 1-1.5$, so $\mu \simeq 2.1-1.4$. The ablation velocity, conduction exponent and ablation front width can be found by applying the fitting procedure outlined in Ref. [19] to one-dimensional simulations.

During the laser trough, until the launch of the second shock, the ablation front widths are roughly constant. Time-averaged values, $\langle L_0 \rangle$, are roughly 0.85, 1.0 and 1.15 μm for the low, nominal and high picket pulses, respectively. Also during this time, the conduction exponent is constant, with $\nu \simeq 1.3$ for all picket values. Additionally, the time-averaged ablation velocities during the laser foot (combined picket and trough) vary with the picket strength. For the low, nominal and high pickets $\langle V_a \rangle \simeq 0.75,\ 1.0,$ and 1.25 μm/ns, respectively. Figure 12 shows the blow-off velocities as a function of mode number during the trough of each laser pulse, as calculated by Eq. 8 with the above-mentioned values of $\langle L_0 \rangle$, ν and $\langle V_a \rangle$. The higher the picket strength, the greater the blow-off and ablation velocities during the early stage of the implosion. Additionally, the stronger pickets set up larger post-shock sound speeds, with $c_s \simeq$ 13.5, 15.5, 17.0 μm/ns for the low, nominal and high pickets.

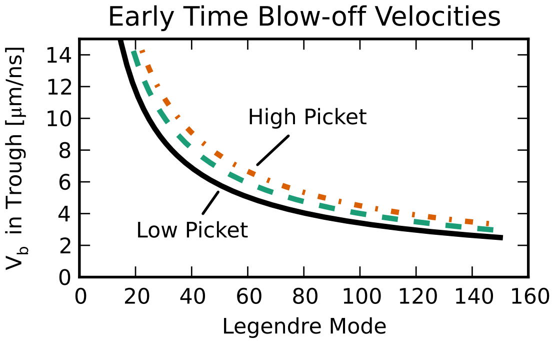

FIG. 12: Blow-off velocities during the trough of each laser pulse.

In total, the different sound speeds, blow-off and ablation velocities change the analytic ablative RM growth factor. Figure 13 shows the zero contours of the ablative RM growth factor, as calculated by Eq. 7 for the three different laser pickets with $k = l/R = l/1100$ μm and assuming the values of $\langle L_0 \rangle$, ν, $\langle V_a \rangle$ and c_s that are valid during the laser

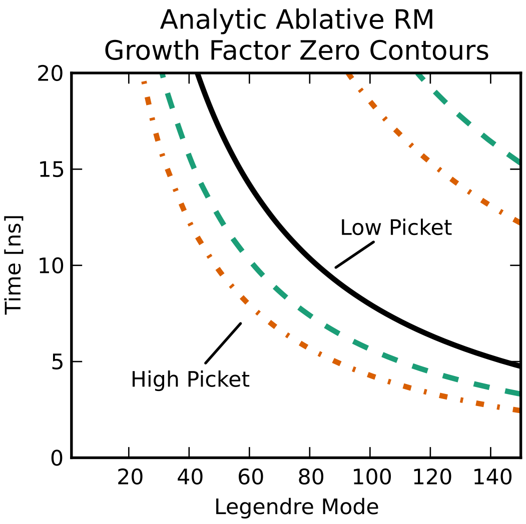

FIG. 13: Growth factor zeros for ablative RM, as calculated by Eq. 7, for the three laser pickets.

trough. The analytic solutions track the results of the growth factor simulations quite well (as seen by comparing to Figure 8).

Figure 13 shows that the shift of the growth factor zero from higher mode number to lower mode number with increasing picket strength can be explained in part by the increased velocities during the ablative RM phase, as set up by the stronger first shock. The oscillatory part of the ablative RM growth factor has a frequency $\omega = k\sqrt{V_a V_b}$, so the first growth factor zero appears in a time $T_0^{\mathrm{RM}} \sim R/l\sqrt{V_a V_b}$. This behavior explains the trajectories of the growth factor zeros seen in the RM phase of the simulations. Higher mode numbers transition to negative growth factors more quickly than do lower mode numbers. Increasing the ablation and blow-off velocities (as happens with a stronger first shock and higher picket strength) causes all mode numbers to become negative sooner, which has the net effect of shifting the growth factor zero contour to lower mode number.

Figure 13 also shows that the late-time evolution of the ablation front growth factor cannot be explained by ablative RM alone. The simulations show that once the ablation front begins to accelerate the growth factor zero quickly moves to higher mode number before locking in for the duration of the implosion. The ablative RM formula, Eq. 7, does not capture this behavior.

After the rarefaction from shock 1 returns to the ablation front, the ablation front begins to accelerate and experiences ablative Rayleigh-Taylor growth, which is a competition between an exponentially growing and decaying solution:

$$\eta(k,t) = Ae^{\gamma t} + Be^{-\gamma t}. \tag{10}$$

One approximation to the ablative Rayleigh-Taylor growth rate $\gamma(k)$ for indirectly driven systems is [1, 2, 19]

$$\gamma(k) = \sqrt{\frac{A_t g k}{1 + kL_m}} - 1.4 V_a k, \tag{11}$$

which depends on the Atwood number A_t, the ablation front acceleration g and the minimum ablation front scale length $L_m = L_0(\nu+1)^{\nu+1}/\nu^{\nu}$. The constants A and B are determined by the initial conditions at the ablation front at the onset of RT growth, at $t = t_{\mathrm{RT}}$. These are $\eta_0(k) = \eta(k, t = t_{\mathrm{RT}})$ and $\eta_0'(k) = \partial\eta/\partial t(k, t_{\mathrm{RT}})$, so that

$$A(k) \;=\; \left(\eta_0 + \frac{\eta_0'}{\gamma}\right) \tag{12}$$

$$B(k) \;=\; \left(\eta_0 - \frac{\eta_0'}{\gamma}\right). \tag{13}$$

At the onset of RT growth, the ablation front has already undergone ablative RM oscillations, so that $\eta_0(k) = \eta_{\mathrm{ARM}}(k, t_{\mathrm{RT}})$, as given by Eq. 7.

Ultimately, we are interested in the mode for which the ablation front growth factor is zero at the time of peak velocity, t_{peak}, $l_0 = k_0 R$, so that $\eta(k_0, t_{\mathrm{peak}}) = 0$. Before peak velocity, the growing and decaying solutions compete, but as $t \to \infty$, the growing solution dominates. Therefore, the condition $A(k_0) = 0$ determines k_0. This can be re-written as the condition $\chi(k_0) = -1$, where

$$\chi(k) = \frac{\eta_0'}{\eta_0 \gamma}. \tag{14}$$

Equation 14 shows that the location of the growth factor zero at peak velocity depends on the growth factor before acceleration begins, the change in growth factor at the start of that acceleration and the RT growth rate.

Setting Eq. 10 equal to zero and solving for t gives the trajectory of the growth factor zero as a function of time during RT growth:

$$T_0^{\mathrm{RT}}(k) = \frac{1}{2\gamma} \ln \left[\frac{\chi - 1}{\chi + 1} \right] + t_{\mathrm{RT}}. \tag{15}$$

Eq. 15 also shows that $\chi(k_0) = -1$ determines the final growth factor zero, as T_0^{RT} asymptotes at $k = k_0$. The salient point is that the location of the growth factor zero at peak velocity depends uniquely on χ, which is a function of the state of the ablation surface at the end of the RM phase (η_0), the RT growth rate γ and the perturbation given to the ablation front at the start of peak acceleration, $\eta_0' \simeq \left[\eta(t_{\mathrm{RT}} + \Delta t) - \eta(t_{\mathrm{RT}}) \right] / \Delta t \doteq (\eta_1 - \eta_0)/\Delta t$.

The time-dependent nature of the ablation surface complicates the analysis, since g ramps up over a finite period of time before it reaches a ~ 1 ns long constant maximum of ~ 100 μm/ns^2. This happens when the ablation front is at lab-frame radius of approximately 800 μm. In order to use the constant-acceleration solution of RT growth (Eq. 10), let us define the start of RT as the beginning of the constant peak acceleration. At this time $R \simeq 800$ μm and $g \simeq 100$ μm/ns^2. The ablation velocity is 14 μm/ns. Since the density gradient scale lengths for these designs are small (~ 10 μm), we ignore the L_m term in the growth rate. Under these circumstances, we can estimate the trajectory of the late-time growth factor zero crossing with Eq. 15, using η_0 and η_0' from the simulations at this time as initial conditions. Figure 14 shows $\eta_0' \Delta t$ from the simulations using $\Delta t = 0.1$ ns.

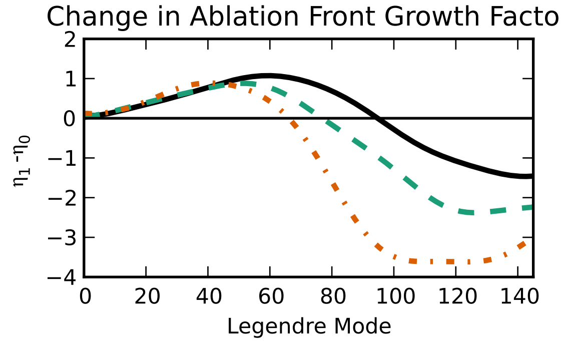

FIG. 14: The change in ablation front growth factor as extracted from the three simulations during the first 0.1 ns of the RT phase, so that $\eta_0' = (\eta_1 - \eta_0)/(0.1 \text{ ns})$.

Figure 15 shows the growth factor zero crossing trajectories as extracted from each of the simulations as well as calculated with Eq. 15. The agreement in all three cases strongly suggests that Eq. 15 is a good estimate for the growth factor zero trajectory. It also suggests that $\chi = -1$ gives the correct mode number for the peak velocity growth factor zero. Therefore, the peak velocity growth factor zero location depends only on η_0 (which can be described by Eq. 7 at $t = t_{\mathrm{RT}}$), γ (Eq. 11) and η_0'.

Taken together, Figures 13 and 15 illustrate that the behavior of the ablation surface can be described by RM growth early in time and RT growth late in time. The return of the ice-gas rarefaction to the ablation surface separates these two time periods.

The influence of the capsule interior is necessary to bridge the gap between the end of RM growth and the start of RT growth. The growth factor simulations show how shocks launched from the ablation surface collectively combine

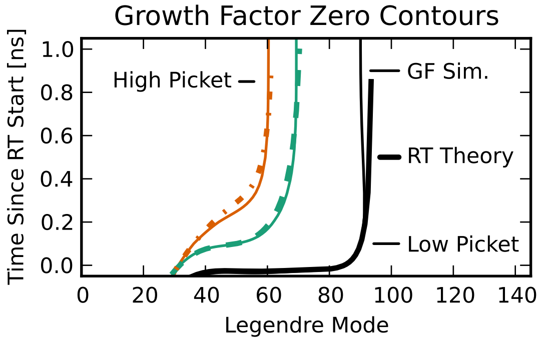

FIG. 15: Theoretical and simulated growth factor zeros as a function of time beginning at the start of peak acceleration for the three laser pickets. Thin lines are from the simulations, thick lines are Eq. 15.

and perturb the region within the ablator (between the ablation surface and the fuel-ablator interface). During the main acceleration phase the ablation front enters and interacts with this pre-perturbed capsule. We make the ansatz that this interaction determines η_0', which is given by the difference in the perturbed ablator and the perturbed ablation front during acceleration over a time period given by the magnitude of the RT growth rate. Furthermore, we suppose that the perturbation inside the ablator is the sum of n perturbed shocks that are launched from the ablation surface and that oscillate for some time until they reach the location inside the capsule where the ablation surface will be at peak acceleration.

Given these assumptions we can develop a model for the ablation front growth factors at all times. Before the launch of the final shock at time t_l^n, the growth is given by the ablative RM oscillations (Eq. 7) as set up by the first shock. After this time, the ablation surface evolves according to the ablative RT equations (Eq. 10) with initial conditions given by the state of the ablation front at the final shock launch time and by the interior capsule perturbation, as set up by shocks launched from the ablation surface:

$$\eta\left(t\right) \simeq \begin{cases} \eta_{\mathrm{ARM}}^{\mathrm{Shock}\ 1}\left(t\right) & t < t_l^n, \\ \eta_{\mathrm{RT}}\left(t, \eta_0, \eta_0', \gamma\right) & t > t_l^n, \end{cases} \tag{16}$$

with

$$\eta_0 \simeq \hat{\eta}_0 = \eta_{\mathrm{ARM}}\left(t_l^n\right), \tag{17}$$

$$\eta_0' \simeq \hat{\eta}_0' = \frac{\hat{\eta}_1 - \hat{\eta}_0}{\Delta t} \simeq \left(\hat{\eta}_1 - \hat{\eta}_0\right)\left|\gamma\right|, \tag{18}$$

$$\eta_1 \simeq \hat{\eta}_1 = \sum_i^n \eta_{\mathrm{ARM}}\left(t_l^i\right) \frac{\sin k c_i t_{\Delta r}^i}{k c_s^i t_{\Delta r}^i}. \tag{19}$$

To be explicit, our analytic approximations to η_0, η_1 and η_0' are respectively $\hat{\eta}_0$, $\hat{\eta}_1$ and $\hat{\eta}_0'$. At the time of peak acceleration the ablation front is at a Lagrangian radius r_p. Each shock transits from the ablation surface at time t_l^i to r_p in a time $t_{\Delta r}^i$. During this time, the shock takes the perturbation on the ablation surface at shock launch time $\eta_{\mathrm{ARM}}(t_l^i)$ and changes it via the damped oscillatory term in Eq. 19. The capsule at r_p is perturbed by the transiting shock and does not change until another shock transits, at which time the subsequent shock linearly adds to the existing perturbation. RT growth is determined by the interaction between the ablation surface (which is in state $\hat{\eta}_0$) and the shock-perturbed ablator interior at r_p (which is in state $\hat{\eta}_1$). The important parameters in this model are the ablation and blowoff velocities after shock 1, the post-shock sound speeds, the shock launch times, the shock transit times to the peak acceleration ablation front radius (~ 800 μm in the laboratory frame), and the RT growth rates, which depend on the late-time acceleration and ablation velocities.

We now test our model on the nominal picket case. In addition to those parameters already listed, Eq. 16 requires shock launch times t_l^i, post-shock sound speeds c_s^i, and oscillation times $t_{\Delta r}^i$. These parameters are listed alongside post-shock ablation velocities V_a^i, ablation front widths L_0^i and thermal conduction exponents ν^i in Table II. Clearly, the ablation front is evolving in time. For now, we ignore the effects of later time shocks on the ablative RM oscillation and approximate $\eta_{\mathrm{ARM}} \simeq \eta_{\mathrm{ARM}}^{\mathrm{Shock}\ 1}$. We explore time dependence below.

TABLE II: Shock parameters as extracted from the 1D nominal picket simulation. Units are ns and μm.

Shock Number i	1	2	3	4	5
t_l^i	0.0	13.5	15.4	16.8	18.1
$t_{\Delta r}^i$	6.5	1.4	0.8	0.4	0.2
c_s^i	15.5	17.5	20.0	35.0	40.0
V_a^i	1.0	1.6	2.0	14.0	15.0
L_0^i	1.0	0.3	0.4	0.4	1.0
ν^i	1.3	1.5	1.7	2.0	2.0

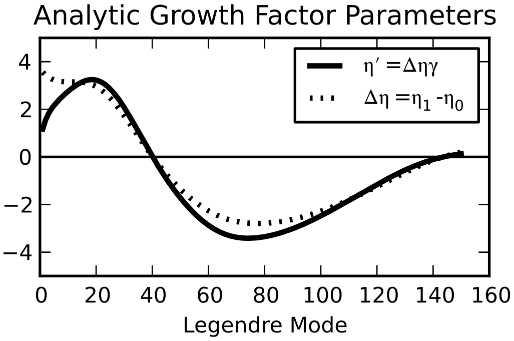

FIG. 16: The growth factor parameters η_0' and $\eta_1 - \eta_0$ as approximated analytically by $\hat{\eta}_0'$, $\hat{\eta}_1$ and $\hat{\eta}_0$ using equations 17 - 19.

Figure 16 shows η_0' and $\eta_0 - \eta_1$ as approximated by $\hat{\eta}_0'$, $\hat{\eta}_0$ and $\hat{\eta}_1$ in equations 17 - 19 using the nominal picket parameters. It is noteworthy that our analytically estimated η_0' is qualitatively very similar to the $\eta_0'\Delta t$ extracted from the nominal picket simulation and shown in Figure 14. However, quantitatively, the analytic $\eta_1 - \eta_0$ is larger than that extracted from the simulations (ranging from -4 to +3, instead of -2.5 to +1), and the zero crossing location is at lower mode number (40 as opposed to 80).

Figure 17 shows the model ablation growth factor spectra, Eq. 16, for parameters similar to the nominal picket simulation. The model ablation front growth factors capture many of the qualitative features present in the full simulation of Figure 7. Both the slow ablative RM oscillations and the sharp "backtracking" in the zero-crossing during the RT phase appear. Additionally, the amplitude of the growth factor is similar. However, the model does not capture all of the dynamics of the full simulations, such as the changes in the ablation front growth factor during the launches of shocks 2, 3, and 4. As such, the initial conditions at the onset of RT are not identical, and some differences in the final growth factor zero location are to be expected. Another consequence of the different initial conditions is the model's positive growth near mode 140, which disappears in the full simulation. However, considering the assumptions, the model ablation front growth factors still capture much of the dynamic behavior seen in the full simulations.

Most importantly, the model can show how slight changes caused by laser picket variations translate into differences in peak velocity growth factors. Figure 18 shows the zero-growth contour trajectories as calculated by Eq. 16 for three different values of ablation velocity during the RM phase. The dashed line is the contour for the nominal picket parameters, while the solid and dash-dot lines are the calculated zero-contours for lowering and raising the RM ablation velocity by 50 percent, respectively. Increasing the ablation velocity during the RM phase has the same effects in the model as in the simulations, with the RM and RT zero trajectories moving towards lower mode number.

We now attempt to model the time-dependent nature of the ablation front. Our simulations (and ICF implosions) include multiply launched shocks that influence the ablation front growth factor spectrum (see Fig. 7). Miklaelian [20] observed that for classical RM a re-shocked interface will continue to evolve as before but with an additional component that depends on the change in the interface's velocity after re-shock Δv. If $\Delta v = 0$, the interface continues evolving as if the re-shock never took place. After the time of re-shock, the interface's perturbation continues to evolve linearly in time, but with a new slope that has an additional component that is proportional to Δv and the amplitude of the perturbation at the time of re-shock. That is, a re-shock adds a component to the pre-existing RM oscillation that starts at zero and evolves at a rate that depends on the velocity change induced by the second shock, so that the amplitude is continuous as a function of time.

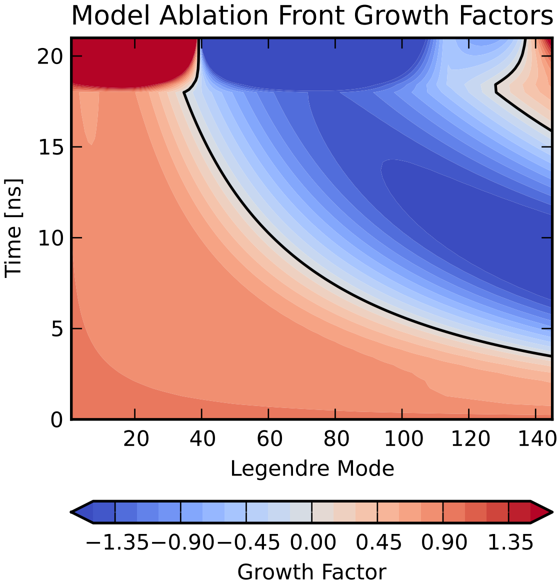

FIG. 17: Model ablation front growth factors as a function of mode number and time as calculated by Eq. 16 for parameters similar to the nominal picket simulation.

To include the effects of multiple shocks, we adopt a similar prescription, so that each subsequent shock adds a component to the ablation front growth factor that is proportional to the growth factor at time of shock launch and grows according to the difference in ablation velocity imparted by the subsequent shock. Additionally, because $\eta_{\mathrm{ARM}}(t=0)=1$, we subtract 1 from the additional component for continuity of growth factor.

$$\eta_{\mathrm{ARM}}(t)=\sum_i \eta_{\mathrm{ARM}}\left(t_l^i\right)\left[\eta_{\mathrm{ARM}}(t-t_l^i, V_a^i-V_a^{i-1}, c_s^i, V_b^i)-1\right]. \tag{20}$$

In cases where a shock doesn't change the ablation velocity, the first term in brackets in Eq. 20 is 1, so no contribution is added to the growth factor. This is also true at $t=t_l^i$, ensuring continuity.

Figure 19 shows the ablation front growth factors using the many shock RM model of Eq. 20. The new model more faithfully captures the simulation dynamics as compared to the single RM case of Fig. 17. In particular, the addition of shocks 2 and 3 keep the higher modes ($l>100$) from becoming positive before the launch of shock 4. Additionally, after shock 4, the first zero crossing quickly moves to lower mode number as a brief higher mode positive oscillation appears, and then quickly disappears, as in the simulation. However, the analytic model does not capture all of the dynamics of the simulations, such as the brief changes in the zero contour at the launching of shocks 2 and 3, which may indicate that our time-dependent, multi-shock prescription could use improvement.

In any case, the improved fidelity by including the effects of multiple shocks also appears in Fig. 20, a repeat of the shock 1 V_a scan in Fig. 18, but with the multiple-shock RM model. As in the simulations of the three picket pulses, the zero crossing contour for all values of V_a^1 moves to around mode 20 after the launch of the fourth shock. This suggests that this behavior comes from the influence of the fourth shock on the ablation front growth factor.

Interestingly enough, the lowest mode zero crossing appears to be insensitive to the inclusion of multiple shocks in the RM formula; the final zero locations in Figs. 20 and 18 are nearly identical. (At high modes, however, this is not the case, as the single shock formula displays the aforementioned positive oscillation.)

Our analytic model of coupled RM-RT growth can also provide insight into the sensitivity to some 1D parameters. Firstly, we note that the condition on the final zero crossing $\chi=\eta_0'/\eta_0\gamma=-1$ is equivalent to $\eta_1=0$, since we let $\eta_0'=(\eta_1-\eta_0)|\gamma|$. The growth factor at late time $t\gg t_l^n$ is dominated by the growing mode and is roughly $\eta_1\exp(\gamma(t-t_l^n))$. To simplify η_1, we note that the oscillatory factor in Eq. 19 is nearly unity for all shocks except shock 1 due to the small oscillation time. Additionally, for shock 1 $\eta_{\mathrm{ARM}}(t_l^1=0)=1$. As such, a simpler model of η_1 is

$$\eta_1\simeq\frac{\sin kc_s^1t_{\Delta r}^1}{kc_s^1t_{\Delta r}^1}+\sum_{i=2}^n \eta_{\mathrm{ARM}}(t_l^i). \tag{21}$$

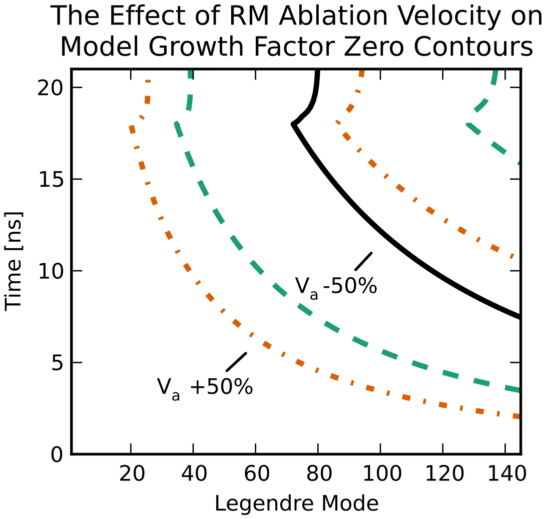

FIG. 18: Growth factor zero trajectories as calculated by the model of Eq. 16. The dashed line is the zero contour for the same parameters as in Fig. 17. The solid and dash-dot lines respectively represent lowering and raising the RM ablation velocity by 50%.

To further simplify, we take the model whereby the ablation front growth factor is only given by shock 1, which is slowly varying in time after the launch of shock 2 (as seen in Fig. 17). This supposition is further supported by the similarity of the final growth factor zero location in the single shock and multiple shock RM models. Therefore, we set $\eta_{\mathrm{ARM}}(t_l^i) = \eta_{\mathrm{ARM}}(t_l^2)$. As such, the seed for RT growth can be approximated by

$$\eta_1 \simeq \frac{\sin kc_s^1 t_{\Delta r}^1}{kc_s^1 t_{\Delta r}^1} + (n-1)\eta_{\mathrm{ARM}}(t_l^2). \tag{22}$$

Equation 22 supports the intuition that the seed for RT growth scales linearly with number of shocks, especially because the second term is much larger than the first, even for $n = 2$. Therefore, absent a change in the RT growth, designs with five shocks would be expected to have 33% more growth than designs with four shocks. Similarly, designs with 3 shocks would have 33% less growth. Interestingly enough, the strength of the first shock is important insofar as it sets the zero of η_{ARM}.

To quantify how the strength of the first shock can alter the growth factor zero location we perform a sensitivity study of the zero of Eq. 22 by independently varying the parameters $\{t_l^2, t_{\Delta r}^1, c_s^1, V_a^1, L_0^1, \nu^1\}$ about their nominal values of Table II and fitting each sensitivity to a power law. We find that the growth factor zero is most sensitive to the post-shock ablation velocity ($\sim (V_a^1)^{-1.49}$), the length of the trough ($\sim (t_l^2)^{-0.94}$) and the post-shock sound speed ($\sim (c_s^1)^{0.20}$). The other parameters are sub-dominant, ($\sim (\nu^1)^{-0.09}, \sim (L_0^1)^{-0.05}, \sim (t_{\Delta r}^1)^{0.01}$). As such, we can combine the main trends from Eq. 22 into a single scaling law for the mode number with zero growth factor, l_0:

$$l_0 \sim V_a^{-1.49} t_l^{-0.94} c_s^{0.2}, \tag{23}$$

in which we have dropped the superscripts for simplicity, but V_a and c_s are the post-first shock ablation velocity and sound speed, and t_l is the time of the second shock's launch.

These scalings help explain the trends seen in the full growth factor simulations. As compared to the nominal picket, V_a is 25% higher (25% lower) for the high (low) picket pulses. Similarly, c_s is 10% higher (13% lower), and t_l is 17% lower (7% higher). Therefore, the scaling in Eq. 23, suggests that the high (low) picket cases should have a growth factor zero that is 0.87 (1.40) times the nominal picket value of 69, or 60 (97). These values are comparable to the growth factor simulations' values of 61 for the high picket and 91 for the low picket case.

The zero crossing scaling might also help explain why the final zero from the nominal picket simulations is higher than predicted by the analytic model. The laser picket causes the ablation front to change significantly during the first few nanoseconds of the pulse. This motivates excluding the laser picket from the analysis and focusing on the

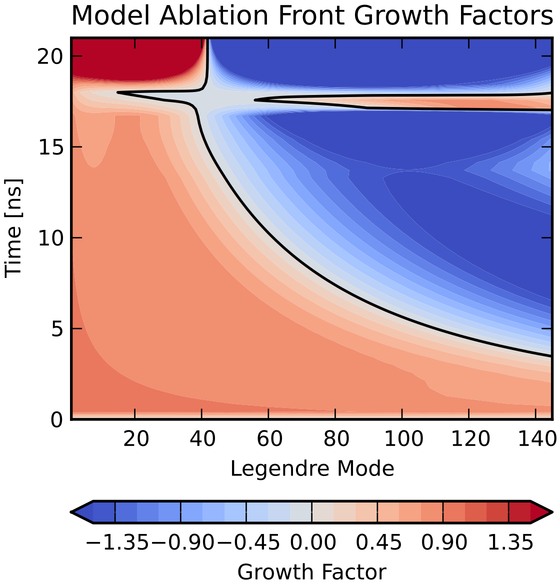

FIG. 19: Model ablation front growth factors as a function of mode number and time as calculated with the many shock RM model of Eq. 20 for parameters similar to the nominal picket simulation.

relatively steady state of the laser trough, effectively shifting the start time of the analysis to the start of the laser trough. This is consistent with the findings in Ref. [18] of a breakdown of the ablative RM model early time, as the ablation front establishes itself. By ignoring the laser picket, the trough-averaged ablation velocity is 0.9 μm/ns, instead of 1.0 ns. (The low and high picket cases change by similar amounts.) Additionally, t_l is effectively 3 ns shorter, if the ablation front oscillations start at the end of the laser picket instead of the start. This implies t_l should be 10.5 ns instead of 13.5 ns. Therefore, Eq. 23 says that the growth factor zero at 42 should be 1.48 times higher, or 62, which is much closer to the simulations value of 69. This scaling estimate is consistent with the multi-shock analytic growth factor spectrum in Fig. 21 that has $l_0 = 58$, in which we have set $t_l^1 = 3$ ns, $V_a^1 = 0.9$ μm/ns, and $\eta(t < t_l^1) = 1.0$.

Taken as a whole, our simulations and model show that implosions with stronger first shocks have zero-crossings at lower mode number because of an increased ablative RM oscillation frequency. The effects of early-time drive on peak-velocity growth factors comes from the launching of later-time shocks, which carry the surface RM oscillation and imprint the entire ablator with a perturbation before the onset of RT growth.

V. CONCLUSIONS

Hydrodynamic growth in NIF ignition capsules involves the interplay of the Richtmyer-Meshkov and Rayleigh-Taylor instabilities. This interaction determines whether surface perturbations grow inward or outward by the time of peak implosion velocity. Simulations of NIF implosions show that the strength of the first shock can alter the modal demarcation between positive and negative linear growth.

Our growth factor simulations show complex time-dependent behavior, but the physical process appears relatively simple: everything flows from the ablation surface. The first shock sets up an ablative Richtmyer-Meshkov oscillation on the ablation surface. Subsequent shocks carry this RM information and perturb the capsule interior, ahead of the ablation front. As the ablation surface begins to accelerate, it experiences an effective “growth factor velocity perturbation” (η_0') from entering the wakes of these previously launched shocks. This perturbation strikes the ablation surface, which then experiences ablative RT growth until peak velocity. The interaction of the ablation surface and the perturbed capsule interior determines the final location of the ablation front growth zero.

It should be noted that our simulations show evolution that is dominated by the ablation front, and that hydrodynamic growth in implosions whose interior interfaces are more unstable could be more complex.

We have developed a simple analytic model for the growth at the ablation surface that captures some of the key

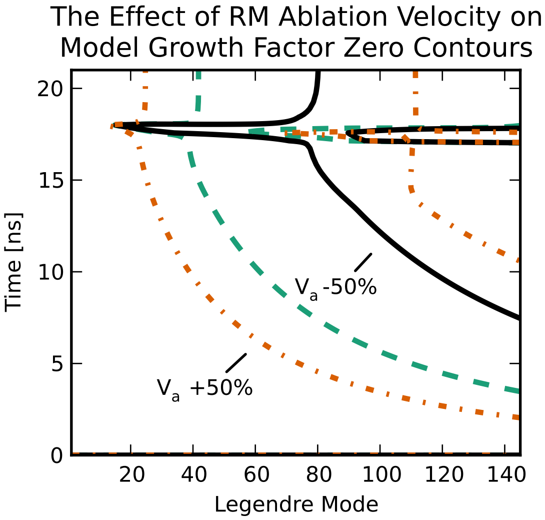

FIG. 20: Growth factor zero trajectories as calculated by the many shock RM model using Eq. 20. The dashed line is the zero contour for the same parameters as in Fig. 17. The solid and dash-dot lines respectively represent lowering and raising the RM ablation velocity by 50%.

dynamics of the simulations. In particular, we have shown how stronger first shocks lead to faster ablative RM oscillations, which translate to a lower mode number for zero growth throughout the entire implosion. This behavior may help explain why measurements of NIF capsule growth with "high foot" pulses have near zero growth at mode 90, where "low foot" pulses have positive growth [11, 21–23]. Furthermore, the experimental data suggest that the low foot has l_0 at much higher mode number than the point design of our simulations. This behavior is consistent with the reduced effective drive necessary to match shock timing measurements [24]; a weaker early time ablation velocity pushes l_0 to higher mode number.

Our model provides a framework for exploring such effects as the number of launched shocks and shock timings on growth factor zero locations. The simple analytic model illustrates that the length of the laser trough and the ablation velocity and sound speed during that time are largely responsible for setting the mode that will have zero growth during late time acceleration. A scaling law based on these three parameters captures the relative difference seen in full radiation-hydrodynamic simulations of capsule implosions with different laser pulses. The number of shocks appears important in-so-far as each shock after the first linearly adds to the seed perturbation.

Interestingly enough, the dynamics of our simulations complicate the picture of RT feed-through from the ablation surface to the capsule interior [1]. This is because late-time shocks carry the perturbations volumetrically throughout the capsule ahead of the ablation surface. Figure 10 shows that by peak implosion velocity, the growth factor on the inside of the ablation surface does not appear to follow the simple $\sim \exp(-k\Delta x)$ relationship expected from pure RT feed-through from the ablation surface. Since the late-time shocks bring the ablation surface perturbation to the capsule interior, the perturbations on the inner ablator surfaces are coupled to those on the ablation front before the onset of RT growth. Certainly the RT ablation front growth feeds-through to the capsule interior and interacts with the perturbation already there, but merely increasing the thickness of the capsule ablator might not de-couple ablation front and fuel-ablator growth. That is, even with a very thick ablator, shocks can still bring ablation front perturbations to interior interfaces. Should interior capsule interfaces be unstable during acceleration or deceleration, seeds that originated on the ablation surface can grow on the fuel-ablator interface, even if the ablator is still very thick.

Finally, it may be possible to use the trends in this work to engineer the location of l_0, by using the first shock to place it either at the statistical peak of surface perturbations (per Fig. 1), or at the peak of the RT growth spectrum. An investigation of this possibility seems worthwhile.

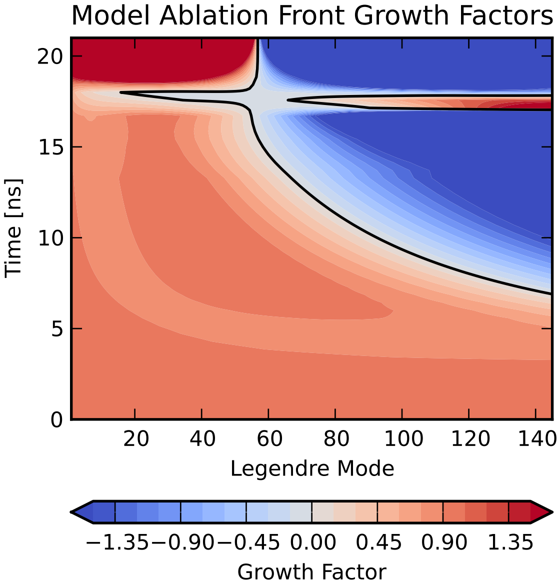

FIG. 21: Ablation front growth factor spectrum using the multi-shock prescription of Eq. 20 and the nominal picket parameters in Tab. II, but with $t_l^1 = 3$ ns and $V_a^1 = 0.9$ μm/ns, which start the analysis after the laser picket.

Acknowledgments

The authors would like to thank K. O. Mikaelian and H. F. Robey for useful discussions. This work was performed under the auspices of the U.S. Department of Energy by Lawrence Livermore National Laboratory under Contract DE-AC52-07NA27344.

Appendix

For a planar system undergoing ablative RM oscillations [18], the growth factor of mode k can be described analytically as

$$\eta_{\mathrm{ARM}}(k,t) = -N_1\left(1+\Upsilon\right)\left[\int_0^{kc_st} dt' \int_0^{t'} dt'' J_0(t'') + J_0(kc_st) - kc_st\right] \\ -4N_1\Upsilon\frac{J_1(kc_st)}{kc_st} + e^{-2kV_at}\left[\alpha_0\cos\left(\omega t\right) + \beta_0\sin\left(\omega t\right)\right] + \eta_\Omega, \tag{A24}$$

In general, Eq. A24 describes an oscillation of frequency $\omega(k) = k\sqrt{V_aV_b}$ that depends on the ablation velocity V_a and the velocity of the blow-off plasma V_b. The post-shock sound speed is c_s, and J_0 and J_1 are Bessel functions. The first shock's vorticity contributes η_Ω. We now apply the parameters of our simulations to derive Eq. 7 from Eq. A24, describing N_1, Υ, α_0, β_0 and η_Ω in turn.

The N_1 and Υ functions depend on the shock Mach numbers in the laboratory and post-shock fluid frames, M_s and M_1, and the density jump due to the shock R:

$$\Upsilon = \frac{\left(1-M_1^2\right)\left(1+3M_s^{-2}\right)}{\left(3+M_1^2\right)\left(1+M_s^{-2}\right)+2\left(1+3M_1^2\right)}, \tag{A25}$$

$$N_1 = -4\frac{M_1^2\left(R-1\right)}{3+M_s^{-2}}. \tag{A26}$$

The fluid-frame Mach number M_1 is related to the shock Mach number M_s by

$$M_s^2 = \frac{M_1^2 R}{(1+R)M_1^2 - 1}. \tag{A27}$$

In our simulations, the ablation front RM oscillation is set by the strong first shock, with $R \simeq 3$ and $M_s^2 \gg 1$, so

$$M_1 \simeq \sqrt{\frac{1}{1+R}} = \frac{1}{2}. \tag{A28}$$

Therefore, N_1 and Υ reduce to

$$\begin{aligned} N_1 &\simeq -\frac{4}{3}\left(\frac{R-1}{R+1}\right) = -\frac{2}{3}, && \text{(A29)} \\ \Upsilon &\simeq \frac{R}{12+5R} = \frac{1}{9}. && \text{(A30)} \end{aligned}$$

Other terms in the ablation front growth factor are the constants α_0 and β_0:

$$\begin{aligned} \alpha_0 &= 1 + N_1(1+3\Upsilon) - \eta_\Omega(0), && \text{(A31)} \\ \beta_0 &= -N_1(1+\Upsilon)\tfrac{c_s}{\sqrt{V_a V_b}} + \sqrt{\tfrac{V_a}{V_b}}\left[\tfrac{\eta_0'}{kV_a\eta_0} + 2 + 2N_1(1+3\Upsilon) - 3\eta_\Omega(0)\right], && \text{(A32)} \\ \frac{\eta_0'}{kV_a\eta_0} &\simeq -\left[\tfrac{R+1}{2} + \tfrac{1}{2M_1}\left(\tfrac{V_b}{c_s} - \tfrac{N_1 c_s}{2V_b}\right)\right] = -\left[2 + \tfrac{V_b}{c_s} + \tfrac{c_s}{3V_b}\right], && \text{(A33)} \\ \eta_\Omega(0) &\simeq N_1 \tfrac{c_s}{V_b}\tfrac{M_1(R-1)}{1+M_1}\left[1 + \Upsilon\tfrac{M_1^2+3}{(1+M_1)^2}\right] = -\left(\tfrac{376}{729}\right)\tfrac{c_s}{V_b}. && \text{(A34)} \end{aligned}$$

So that α_0 and β_0 reduce to

$$\alpha_0 \simeq \frac{1}{9} + \left(\frac{376}{729}\right)\frac{c_s}{V_b}, \tag{A35}$$

and

$$\beta_0 \simeq \frac{20}{27}\frac{c_s}{\sqrt{V_a V_b}} + \sqrt{\frac{V_a}{V_b}}\left[-\frac{16}{9} - \frac{V_b}{c_s} + \left(\frac{295}{243}\right)\frac{c_s}{V_b}\right]. \tag{A36}$$

The contribution to the ablation front growth factor from vorticity deposited by the first shock, $\eta_\Omega(k,t)$, is given by [18]

$$\begin{gathered} \eta_\Omega(k,t) \simeq N_1 \frac{c_s}{V_b}\frac{1-M_s^{-2}}{1-M_1^2} M_1\,(R-1)\,e^{kV_a t} \times \\ \int_{kV_a t/|\sinh\theta_s|}^{\infty} e^{-\eta|\sinh\theta_s|}\left[J_1(\eta) + \Upsilon\frac{M_1^2+3}{1-M_1^2}J_3(\eta)\right]d\eta, \end{gathered} \tag{A37}$$

which depends on the function θ_s:

$$\theta_s = \tanh^{-1}\sqrt{\frac{2+(\gamma-1)\,M_s^2}{2\gamma M_s^2 - (\gamma-1)}}. \tag{A38}$$

The ratio of specific heats γ can be determined from the change in density due to the strong first shock:

$$\frac{\gamma+1}{\gamma-1} \sim R. \tag{A39}$$

Since $R \simeq 3$, $\gamma = 2$. In our simulations, the first shock is strong, with $M_s^2 \gg \gamma \sim \mathcal{O}(1)$, so θ_s can be reduced:

$$\theta_s \simeq \tanh^{-1}\sqrt{\frac{(\gamma-1)}{2\gamma}}. \tag{A40}$$

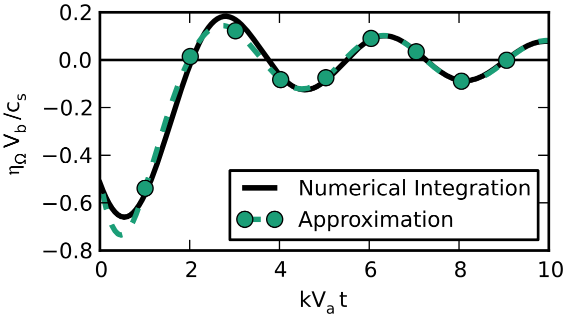

FIG. 22: Vorticity contributions to the ablative RM growth factor from numerically integrating Eq. A42 or using the approximation in Eq. A45.

Furthermore, since $\sinh(\tanh^{-1}(x)) = x/\sqrt{1-x^2}$,

$$\sinh\theta_s \simeq \sqrt{\frac{\gamma-1}{\gamma+1}} = \frac{1}{\sqrt{3}}. \tag{A41}$$

Then, with a change of integration variables, dropping the M_s^{-2} term, and substituting $N_1 = -2/3$ and $\Upsilon = 1/9$, Eq. A37 simplifies to

$$\eta_\Omega(k,t) \simeq -\frac{8\sqrt{3}}{9}\frac{c_s}{V_b}e^{kV_at}\int_{kV_at}^{\infty} e^{-\tau}\left[J_1\left(\sqrt{3}\tau\right) + \frac{13}{27}J_3\left(\sqrt{3}\tau\right)\right]d\tau. \tag{A42}$$

Substituting Eqs. A29, A30, A35, A36 and A42 into Eq. A24 yields Eq. 7.

The vorticity integral, Eq. A42, can be solved numerically, which we do for all figures in the main text using quadrature integration. But we note that for ease of computation, it can be approximated by recognizing that the integrand has a closed-form solution for $kV_at = 0$:

$$\int_0^{\infty} e^{-\tau}\left[J_1\left(\sqrt{3}\tau\right) + \frac{13}{27}J_3\left(\sqrt{3}\tau\right)\right]d\tau = \frac{47}{81\sqrt{3}}. \tag{A43}$$

The integral from 0 to kV_at is sigmoidal and oscillatory, and can be approximated by a generalized logistic function early in time that oscillates and decays at large values of kV_at:

$$\int_0^{x} e^{-\tau}\left[J_1\left(\sqrt{3}\tau\right) + \frac{13}{27}J_3\left(\sqrt{3}\tau\right)\right]d\tau \simeq \frac{47}{81\sqrt{3}}\left[\frac{1}{1+e^{-3(x-0.55)}} + \frac{\sin\left(x\sqrt{3}\right)}{2e^{x}\sqrt{x}}\right]. \tag{A44}$$

Therefore, the vorticity contribution can be approximated as

$$\eta_\Omega(k,t) \simeq -\frac{376}{729}\frac{c_s}{V_b}e^{kV_at}\left[1 - \frac{1}{1+e^{-3(kV_at-0.55)}} + \frac{\sin\left(kV_at\sqrt{3}\right)}{2e^{kV_at}\sqrt{kV_at}}\right]. \tag{A45}$$

Using Eq. A45 as a substitute for Eq. A42 leads to a small error in the total growth factor at low mode numbers at early time, but is easier to implement numerically. At late time, the vorticity contribution decays as $\sin(kV_at)/\sqrt{kV_at}$, as shown in Ref. [18]. Figure 22 compares Eq. A42 and Eq. A45 and shows that the error from using the approximation are small for relevant values of kV_at.

References

---

[1] J. D. Lindl. Development of the indirect-drive approach to inertial confinement fusion and the target physics basis for ignition and gain. *Physics of Plasmas*, 2(11):3933–4024, 1995.

[2] J. D. Lindl, P. Amendt, R. L. Berger, S. G. Glendinning, S. H. Glenzer, S. W. Haan, R. L. Kauffman, O. L. Landen, and L. J. Suter. The physics basis for ignition using indirect-drive targets on the National Ignition Facility. *Physics of Plasmas*, 11(2):339–491, 2004.

[3] G. H. Miller, E. I. Moses, and C. R. Wuest. The National Ignition Facility. *Optical Engineering*, 43(12):2841–2853, 2004.

[4] S. P. Regan, R. Epstein, B. A. Hammel, L. J. Suter, J. Ralph, H. Scott, M. A. Barrios, D. K. Bradley, D. A. Callahan, C. Cerjan, G. W. Collins, S. N. Dixit, T. Doeppner, M. J. Edwards, D. R. Farley, S. Glenn, S. H. Glenzer, I. E. Golovkin, S. W. Haan, A. Hamza, D. G. Hicks, N. Izumi, J. D. Kilkenny, J. L. Kline, G. A. Kyrala, O. L. Landen, T. Ma, J. J. MacFarlane, R. C. Mancini, R. L. McCrory, N. B. Meezan, D. D. Meyerhofer, A. Nikroo, K. J. Peterson, T. C. Sangster, P. Springer, and R. P. J. Town. Hot-spot mix in ignition-scale implosions on the NIF. *Physics of Plasmas*, 19(5):056307, 2012.

[5] T. Ma, P. K. Patel, N. Izumi, P. T. Springer, M. H. Key, et al. Onset of hydrodynamic mix in high-velocity, highly compressed inertial confinement fusion implosions. *Phys. Rev. Lett.*, 111(8):085004, 2013.

[6] R. D. Richtmyer. Taylor instability in shock acceleration of compressible fluids. *Communications on Pure and Applied Mathematics*, 13(2):297–319, 1960.

[7] E. E. Meshkov. Instability of the interface of two gases accelerated by a shock wave. *Fluid Dynamics*, 4:101–104, 1969.

[8] Rayleigh. Investigation of the character of the equilibrium of an incompressible heavy fluid of variable density. *Proceedings of the London Mathematical Society*, s1-14(1):170–177, 1882.

[9] G. Taylor. The instability of liquid surfaces when accelerated in a direction perpendicular to their planes. i. *Proceedings of the Royal Society of London. Series A. Mathematical and Physical Sciences*, 201(1065):192–196, 1950.

[10] S. W. Haan, J. D. Lindl, D. A. Callahan, D. S. Clark, J. D. Salmonson, B. A. Hammel, L. J. Atherton, R. C. Cook, M. J. Edwards, S. Glenzer, A. V. Hamza, S. P. Hatchett, M. C. Herrmann, D. E. Hinkel, D. D. Ho, H. Huang, O. S. Jones, J. Kline, G. Kyrala, O. L. Landen, B. J. MacGowan, M. M. Marinak, D. D. Meyerhofer, J. L. Milovich, K. A. Moreno, E. I. Moses, D. H. Munro, A. Nikroo, R. E. Olson, K. Peterson, S. M. Pollaine, J. E. Ralph, H. F. Robey, B. K. Spears, P. T. Springer, L. J. Suter, C. A. Thomas, R. P. Town, R. Vesey, S. V. Weber, H. L. Wilkens, and D. C Wilson. Point design targets, specifications, and requirements for the 2010 ignition campaign on the National Ignition Facility. *Physics of Plasmas*, 18(5):051001, 2011.

[11] K. S. Raman, V. A. Smalyuk, D. T. Casey, S. W. Haan, D. E. Hoover, O. A. Hurricane, J. J. Kroll, A. Nikroo, J. L. Peterson, B. A. Remington, H. F. Robey, D. S. Clark, B. A. Hammel, O. L. Landen, M. Marinak, D. H. Munro, K. J. Peterson, and J. D. Salmonson. An in-flight radiography platform to measure hydrodynamic instability growth in inertial confinement fusion capsules at the National Ignition Facility. *Physics of Plasmas*, 21:072710, 2014.

[12] B. A. Hammel, S. W. Haan, D. S. Clark, M. J. Edwards, S. H. Langer, M. M. Marinak, M. V. Patel, J. D. Salmonson, and H. A. Scott. High-mode Rayleigh-Taylor growth in NIF ignition capsules. *High Energy Density Physics*, 6(2):171 – 178, 2010.

[13] B. A. Hammel, H. A. Scott, S. P. Regan, C. Cerjan, D. S. Clark, M. J. Edwards, R. Epstein, S. H. Glenzer, S. W. Haan, N. Izumi, J. A. Koch, G. A. Kyrala, O. L. Landen, S. H. Langer, K. Peterson, V. A. Smalyuk, L. J. Suter, and D. C. Wilson. Diagnosing and controlling mix in National Ignition Facility implosion experiments. *Physics of Plasmas*, 18(5):056310, 2011.

[14] D. S. Clark, S. W. Haan, B. A. Hammel, J. D. Salmonson, D. A. Callahan, and R. P. J. Town. Plastic ablator ignition capsule design for the National Ignition Facility. *Physics of Plasmas*, 17(5):052703, 2010.

[15] D. S. Clark, S. W. Haan, A. W. Cook, M. J. Edwards, B. A. Hammel, J. M. Koning, and M. M. Marinak. Short-wavelength and three-dimensional instability evolution in National Ignition Facility ignition capsule designs. *Physics of Plasmas*, 18(8):082701, 2011.

[16] A. L. Kritcher, R. Town, D. Bradley, D. Clark, B. Spears, O. Jones, S. Haan, P. T. Springer, J. Lindl, R. H. H. Scott, D. Callahan, M. J. Edwards, and O. L. Landen. Metrics for long wavelength asymmetries in inertial confinement fusion implosions on the National Ignition Facility. *Physics of Plasmas*, 21:042708, 2014.

[17] M. M. Marinak, R. E. Tipton, O. L. Landen, T. J. Murphy, P. Amendt, S. W. Haan, S. P. Hatchett, C. J. Keane, R. McEachern, and R. Wallace. Three-dimensional simulations of Nova high growth factor capsule implosion experiments. *Physics of Plasmas*, 3(5):2070–2076, 1996.

[18] V. N. Goncharov, O. V. Gotchev, E. Vianello, T. R. Boehly, J. P. Knauer, P. W. McKenty, P. B. Radha, S. P. Regan, T. C. Sangster, S. Skupsky, V. A. Smalyuk, R. Betti, R. L. McCrory, D. D. Meyerhofer, and C. Cherfils-Clérouin. Early stage of implosion in inertial confinement fusion: Shock timing and perturbation evolution. *Physics of Plasmas*, 13(1):012702, 2006.

[19] R. Betti, V. N. Goncharov, R. L. McCrory, and C. P. Verdon. Growth rates of the ablative Rayleigh–Taylor instability in inertial confinement fusion. *Physics of Plasmas*, 5(5):1446–1454, 1998.

[20] Karnig O. Mikaelian. Richtmyer-Meshkov instabilities in stratified fluids. *Phys. Rev. A*, 31:410–419, 1985.

[21] D. T. Casey, V. A. Smalyuk, K. Raman, J. L. Peterson, L. B. Hopkins, D. A. Callahan, D. S. Clark, E. L. Dewald, T. R. Dittrich, S. W. Haan, D. E. Hinkel, D. Hoover, O. Hurricane, J. J. Kroll, O. L. Landen, A. Moore, A. Nikroo, H.-S. Park, B. A. Remington, H. F. Robey, J. R. Rygg, J. D. Salmonson, R. Tommasini, and K. Widmann. Reduced instability growth with high adiabat ("high foot") implosions at the National Igntion Facility. *Physical Review E*, 90:011102(R), 2014.

[22] V. A. Smalyuk, D. T. Casey, D. S. Clark, M. J. Edwards, S. W. Haan, A. Hamza, D. E. Hoover, W. W. Hsing, O. Hurricane, J. D. Kilkenny, J. Kroll, O. L. Landen, A. Moore, A. Nikroo, L. Peterson, K. Raman, B. A. Remington, H. F. Robey, S. V. Weber, and K. Widmann. First measurements of hydrodynamic instability growth in indirectly driven implosions at ignition-relevant conditions on the National Ignition Facility. *Phys. Rev. Lett.*, 112:185003, 2014.

[23] V. A. Smalyuk, M. A. Barrios, J. A. Caggiano, D. T. Casey, C. J. Cerjan, D. S. Clark, M. J. Edwards, J. A Frenje, M. Gatu-Johnson, V. Y. Glebov, G. Grim, S. W. Haan, B. A. Hammel, A. Hamza, D. E. Hoover, W. W. Hsing, O. Hurricane, J. D. Kilkenny, J. L. Kline, J. P Knauer, J. Kroll, O. L. Landen, J. D. Lindl, T. Ma, J. M. McNaney, M. Mintz, A. Moore, A. Nikroo, T. Parham, J. L. Peterson, R. Petrasso, L. Pickworth, J. E. Pino, K. Raman, S. P. Regan, B. A. Remington, H. F. Robey, D. P. Rowley, D. B. Sayre, R. E. Tipton, S. V. Weber, K. Widmann, D. C. Wilson, and C. B. Yeamans. Hydrodynamic instability growth and mix experiments at the National Ignition Facility. *Physics of Plasmas*, 21:056301, 2014.

[24] D. S. Clark, D. E. Hinkel, D. C. Eder, O. S. Jones, S. W. Haan, B. A. Hammel, M. M. Marinak, J. L. Milovich, H. F. Robey, L. J. Suter, and R. P. J. Town. Detailed implosion modeling of deuterium-tritium layered experiments on the National Ignition Facility. *Physics of Plasmas*, 20:056318, 2013.